

# Non-symmorphic symmetry and field-driven odd-parity pairing in CeRh<sub>2</sub>As<sub>2</sub>

D. C. Cavanagh,<sup>1</sup> T. Shishidou,<sup>2</sup> M. Weinert,<sup>2</sup> P. M. R. Brydon,<sup>3,\*</sup> and Daniel F. Agterberg<sup>2,†</sup>

<sup>1</sup>*Department of Physics, University of Otago, P.O. Box 56, Dunedin 9054, New Zealand*

<sup>2</sup>*Department of Physics, University of Wisconsin, Milwaukee, Wisconsin 53201, USA*

<sup>3</sup>*Department of Physics and MacDiarmid Institute for Advanced Materials and Nanotechnology, University of Otago, P.O. Box 56, Dunedin 9054, New Zealand*

Recently, evidence has emerged for a field-induced even- to odd-parity superconducting phase transition in CeRh<sub>2</sub>As<sub>2</sub> [S. Khim *et al.*, Science **373** 1012 (2021)]. Here we argue that the P4/nmm non-symmorphic crystal structure of CeRh<sub>2</sub>As<sub>2</sub> plays a key role in enabling this transition by ensuring large spin-orbit interactions near the Brillouin zone boundaries, which naturally leads to the required near-degeneracy of the even- and odd-parity channels. We further comment on the relevance of our theory to FeSe, which crystallizes in the same structure.

*Introduction*—The discovery of a transition between two distinct superconducting phases at high magnetic fields in CeRh<sub>2</sub>As<sub>2</sub> [1] has generated great interest [2–6]. Due to the immense upper critical field, this has been widely interpreted as a transition between even- and odd-parity pairing states. Creating odd-parity superconductors is a central goal of quantum materials science as they can host non-trivial topological phenomena [7]. The putative field-induced transition in CeRh<sub>2</sub>As<sub>2</sub> offers a straightforward route to a bulk odd-parity state. As such, it is of great importance to clarify the physics responsible for its remarkable phase diagram.

The even to odd parity transition is enabled by a Rashba-like spin-orbit coupling (SOC) that exists on an inversion ( $I$ ) symmetry breaking sublattice of atoms.  $I$  symmetry transforms one sublattice to the other, with opposite signs for SOC, ensuring the Hamiltonian satisfies a global  $I$  symmetry. However, the even to odd parity transition is also suppressed by hopping between the two sublattices, and so the SOC should be larger than this inter-sublattice hopping for this transition to occur. It is unclear if this condition can be realized in bulk crystals: Indeed, a relatively strong Rashba-like spin texture has been observed in bilayer cuprate Bi2212 [8], but there is no evidence of a field-induced odd-parity state. Since superconductors with this sublattice structure are not uncommon, the rarity of the field-induced transition suggests that additional physics is necessary to explain the phase diagram of CeRh<sub>2</sub>As<sub>2</sub>.

Here we show that the non-symmorphic (NS) structure of CeRh<sub>2</sub>As<sub>2</sub> allows the Rashba-like SOC to be larger than the inter-sublattice hopping, providing an explanation for why this transition is observed. In particular, we show that the NS structure ensures that the SOC energy scale is asymptotically larger than that of the inter-sublattice hopping near the Brillouin zone edges. Provided that a Fermi surface with sufficiently large density of states (DOS) exists near the zone edge, the field-induced even- to odd-parity transition can appear at the

relatively high temperature seen in CeRh<sub>2</sub>As<sub>2</sub>.

The manuscript is organized as follows: First a general argument is given that on the Brillouin zone edge arbitrary superpositions of Kramers degenerate states have the same spin polarization direction, in contrast to Kramers degenerate states at the Brillouin zone center. This remarkable feature reflects the dominance of SOC near the zone edges. We confirm this by examining a  $\mathbf{k} \cdot \mathbf{p}$  theory valid near the zone edge and contrasting it with one valid near the zone center. This explicitly reveals that the SOC is asymptotically smaller than the inter-sublattice hopping near the zone center, but is asymptotically larger near the zone edge. Considering superconductivity originating from an intra-sublattice pairing instability, the dominance of the SOC at the zone edge allows us to qualitatively reproduce the magnetic field-temperature phase diagram of CeRh<sub>2</sub>As<sub>2</sub>, provided that the contribution to the DOS from the Fermi surfaces near the zone edges is sufficiently large. Density functional calculations for CeRh<sub>2</sub>As<sub>2</sub> reveal that this can be the case if electron correlations are included. Finally, since our analysis shows that exotic physics due to strong SOC can be expected generically in NS superconductors, we discuss an additional application of our theory to NS FeSe.

*Non-symmorphic symmetry and spin texture*—In contrast to Kramers degenerate band states at the Brillouin zone center, the NS structure of CeRh<sub>2</sub>As<sub>2</sub> implies that the two-fold Kramers degenerate band states at the zone edge exhibit the same spin polarization direction. To show this, we consider the set of symmetries that keep momenta lying in the zone-center plane  $\mathbf{k}_c = (0, k_y, k_z)$  and the zone-edge plane  $\mathbf{k}_e = (\pi, k_y, k_z)$  unchanged. These include:  $M_x$ , a mirror reflection through the  $\hat{x}$  direction;  $T\tilde{I}$ , where  $T$  is time-reversal symmetry and  $\tilde{I} = \{I|\frac{1}{2}, \frac{1}{2}, 0\}$ ; and their product  $T\tilde{I}M_x$ . Since  $(T\tilde{I})^2 = -1$ , these states exhibit a two-fold Kramers degeneracy denoted as  $|\mathbf{k}_{\nu=e,c}, \pm\rangle \equiv |\nu, \pm\rangle$ . These two-fold degenerate eigenstates are also eigenstates of  $M_x$ , and since  $M_x^2 = -1$ ,  $M_x|\nu, \pm\rangle = e_{\nu,\pm}|\nu, \pm\rangle$  where the  $e_{\nu,\pm}$  are purely imaginary. From the non-symmorphicity and the general result that  $T$  commutes with spatial symmetries, we find  $T\tilde{I}M_x = \{E|100\}M_xT\tilde{I}$ , where  $\{E|100\}$  is an in-

\* philip.brydon@otago.ac.nz

† agterber@uwm.edu

plane translation vector. Importantly,  $\{E|100\}$  becomes 1 for  $k_x = 0$ , and  $-1$  for  $k_x = \pi$ . Hence, for the zone center plane  $M_x(T\tilde{I}|c, \pm) = -e_{c,\pm}(T\tilde{I}|c, \pm)$ , while for the zone-edge plane  $M_x(T\tilde{I}|e, \pm) = e_{e,\pm}(T\tilde{I}|e, \pm)$ . We thus conclude that Kramers degenerate partners at the zone center plane have *opposite* eigenvalues with respect to  $M_x$ , while those at the zone boundary have the *same* eigenvalue with respect to  $M_x$ .

Since the spin operators  $S_y$  and  $S_z$  are odd under  $M_x$ , they will have non-zero matrix elements at the zone-center plane, but all their matrix elements are zero at the zone-edge plane [9]. That is, at the zone edges, all eigenstates have their spins polarized along the  $\pm\hat{x}$  direction. A similar argument can be made for the  $\mathbf{k} = (k_x, \pi, k_z)$  plane, where we find that the states are polarized along the  $\pm\hat{y}$  direction. This implies that the states in the zone-edge plane cannot couple to a  $c$ -axis field, while those in the zone center plane can. As seen below, it is this key difference that enhances the  $c$ -axis Pauli limiting fields and stabilizes a field-induced even- to odd-parity transition for Fermi surfaces near the zone edges relative to those near the zone center.

**$\mathbf{k}\cdot\mathbf{p}$  theories**— To quantify the difference between zone-center and zone-edge Fermi surfaces on superconductivity, we construct  $\mathbf{k}\cdot\mathbf{p}$  theories valid near the  $\Gamma$  point and the M-A Dirac line. (Our results for the M-A Dirac line hold more generally for Fermi surfaces near the zone-edge.) For the  $\Gamma$  point, it suffices to take the small  $\mathbf{k}$  limit of the tight binding theory presented in Ref. [1]. To develop the  $\mathbf{k}\cdot\mathbf{p}$  theory near the M-A Dirac line [10] we use the representations as given on the Bilbao crystallographic server [11].

In both  $\mathbf{k}\cdot\mathbf{p}$  theories the Hamiltonian has the structure

$$H_0 = \epsilon_{00,\mathbf{k}}\tau_0\sigma_0 + \epsilon_{x0,\mathbf{k}}\tau_x\sigma_0 + \epsilon_{y0,\mathbf{k}}\tau_y\sigma_0 + \epsilon_{zx,\mathbf{k}}\tau_z\sigma_x + \epsilon_{zy,\mathbf{k}}\tau_z\sigma_y + \epsilon_{zz,\mathbf{k}}\tau_z\sigma_z. \quad (1)$$

The  $\tau_i$  Pauli matrices encode the sublattice basis composed of two states that are transformed into each other under inversion (e.g., a Ce site basis). The  $\sigma_i$  Pauli matrices encode the spin basis. The first line of Eq. (1) describes spin-independent intra- and inter-sublattice hopping processes, whereas the second line includes the SOC terms.  $I$  symmetry is given by the operator  $\tau_x\sigma_0$  at the  $\Gamma$ , M, and A points. Consequently,  $\epsilon_{00,\mathbf{k}}$  and  $\epsilon_{x0,\mathbf{k}}$  are even in momentum  $\mathbf{k}$ , while the other coefficients are odd. Eq. (1) has the same form as a minimal Hamiltonian for a locally non-centrosymmetric material [12–16]. The Hamiltonian possesses two doubly-degenerate eigenvalues  $\epsilon_{00,\mathbf{k}} \pm \tilde{\epsilon}_{\mathbf{k}}$  where

$$\tilde{\epsilon}_{\mathbf{k}} = \sqrt{\epsilon_{x0,\mathbf{k}}^2 + \epsilon_{y0,\mathbf{k}}^2 + \epsilon_{zx,\mathbf{k}}^2 + \epsilon_{zy,\mathbf{k}}^2 + \epsilon_{zz,\mathbf{k}}^2}. \quad (2)$$

It is convenient to label the two degenerate states in each band by a pseudospin index. Our choice of pseudospin basis is presented in the SM [17].

In Table I we give the momentum dependence of the coefficients  $\epsilon_{\mu\nu,\mathbf{k}}$ . Along the M-A line we expand radially

from the line, i.e.,  $\mathbf{k} = (\pi, \pi, k_z) + (k_x, k_y, 0)$  and expand in  $k_x$  and  $k_y$ . We do not give the form of  $\epsilon_{00,\mathbf{k}}$  since this term does not play an essential role in the physics, and also only keep the lowest non-zero power of  $k_\nu$  in the coefficient of each  $\tau_i\sigma_j$  matrix. The  $\mathbf{k}\cdot\mathbf{p}$  theories reveal several remarkable features of the electronic structure: i) The  $\epsilon_{zz,\mathbf{k}}$  SOC is parametrically smaller than the Rashba-like SOC terms  $\epsilon_{zx,\mathbf{k}}$  and  $\epsilon_{zy,\mathbf{k}}$  (and will henceforth be ignored); ii) Near the M-A Dirac line when  $k_x = 0$ , only the coefficient of  $\tau_z\sigma_x$  is non-zero, a consequence of the NS spin texture presented above; iii) The NS symmetry requires that all coefficients vanish at the M-A Dirac line, and hence the energy bands are four-fold degenerate here.

Importantly, the Rashba SOC terms vanish asymptotically more slowly than the inter-sublattice hopping as the M-A Dirac line is approached. This is reflected in the divergence of the ratio  $\tilde{\alpha}_{\mathbf{k}} = \sqrt{(\epsilon_{zx,\mathbf{k}}^2 + \epsilon_{zy,\mathbf{k}}^2)/(\epsilon_{x0,\mathbf{k}}^2 + \epsilon_{y0,\mathbf{k}}^2)}$  as one approaches the Dirac line. In contrast, only the inter-sublattice hopping  $\epsilon_{x0,\mathbf{k}}$  can be nonzero at the  $\Gamma$  point, which implies that the ratio  $\tilde{\alpha}_{\mathbf{k}}$  vanishes at the zone center. As we shall see,  $\tilde{\alpha}_{\mathbf{k}}$  plays a key role in our theory.

**Zeeman response**— We include a Zeeman field by adding the term  $H_Z = g\mu_B\tau_0\vec{\sigma} \cdot \vec{H}$  to the Hamiltonian Eq. (1). Expressed in the band-pseudospin basis,  $H_Z$  typically has both interband and intraband components. The former are not important in the  $\tilde{\epsilon}_{\mathbf{k}} \gg g\mu|\vec{H}|$  limit; in contrast, the latter lifts the pseudospin degeneracy, acting like an effective pseudospin Zeeman field, which we obtain by projecting  $\tau_0\vec{\sigma}$  onto the pseudospin basis,  $\tau_0\sigma_\mu \rightarrow \tilde{\gamma}_{\mathbf{k}}^\mu \cdot \vec{s}$ . For our choice of pseudospin basis, Zeeman fields parallel (perpendicular) to the  $c$ -axis produce pseudospin fields that are also parallel (perpendicular) to the  $c$ -axis; explicit expressions for the effective  $g$ -factors  $\tilde{\gamma}_{\mathbf{k}}^\mu$  are given in the SM [17]. Moreover, the magnitude of  $\tilde{\gamma}_{\mathbf{k}}^\mu$  is basis-independent and given by

$$|\tilde{\gamma}_{\mathbf{k}}^\mu|^2 = \hat{\epsilon}_{x0,\mathbf{k}}^2 + \hat{\epsilon}_{y0,\mathbf{k}}^2 + \hat{\epsilon}_{z\mu,\mathbf{k}}^2 \quad (3)$$

where  $\hat{\epsilon}_{\mu\nu,\mathbf{k}} = \epsilon_{\mu\nu,\mathbf{k}}/\tilde{\epsilon}_{\mathbf{k}}$ . For a  $c$ -axis field, the pseudospin splitting is controlled by the ratio  $\tilde{\alpha}_{\mathbf{k}}$  as  $|\tilde{\gamma}_{\mathbf{k}}^z| = (1 + \tilde{\alpha}_{\mathbf{k}}^2)^{-1/2}$ . Our  $\mathbf{k}\cdot\mathbf{p}$  theory therefore shows that the pseudospin splitting is maximal near the  $\Gamma$  point, but vanishes as we approach the M-A Dirac line. This reflects the in-plane spin polarization of the band states near the zone edge required by the NS symmetry as discussed above, and implies that the effective  $g$ -factor vanishes on the zone boundary ( $|\tilde{\gamma}_{\mathbf{k}}^z| = 0$ ).

**Superconductivity**— In the standard scenario for the field-induced transition in locally  $I$ -symmetry broken superconductors [18–21], the dominant interaction pairs electrons on the same sublattice in a spin singlet. Since the sublattices are swapped by  $I$ , this generates both even- and odd-parity states, corresponding to equal and opposite signs of the pairing potential on each sublattice, respectively. We refer to these two possibilities as the uniform and staggered states. The sign difference can be readily encoded in the  $\tau$ -dependence of the pair-

Γ point		M-A Dirac line
$\epsilon_{x0,\mathbf{k}}$	$g_{x0}$	$m_{x0}^{(e)} k_x k_y$
$\epsilon_{y0,\mathbf{k}}$	$g_{y0} k_z$	$m_{y0}^{(o)} k_x k_y$
$\epsilon_{zx,\mathbf{k}}$	$g_{zx} k_y$	$m_{zx}^{(e)} k_y$
$\epsilon_{zy,\mathbf{k}}$	$-g_{zx} k_x$	$-m_{zx}^{(e)} k_x$
$\epsilon_{zz,\mathbf{k}}$	$g_{zz} k_x k_y (k_x^2 - k_y^2)$	$m_{zz}^{(o)} k_x k_y (k_x^2 - k_y^2)$
$\tilde{\alpha}_{\mathbf{k}}^2$	$\frac{g_{xz}^2 (k_x^2 + k_y^2)}{g_{x0}^2} \rightarrow 0$	$\frac{m_{zz}^{(e)2} (k_x^2 + k_y^2)}{(m_{x0}^{(e)2} + m_{y0}^{(o)2}) k_x^2 k_y^2} \rightarrow \infty$

TABLE I. Form of the nontrivial terms in Eq. (1) near the  $\Gamma$  point and along the M-A Dirac line. The expansion coefficients  $m_{ij}^{(e)}$  are functions of  $k_z$ , with the (e) and (o) superscripts indicating that these are non-vanishing or vanishing at the M and A points. The last row gives  $\tilde{\alpha}_{\mathbf{k}}^2$ , characterizing the ratio of the SOC to the inter-sublattice hopping, and the limiting values as  $\mathbf{k} \rightarrow 0$ .

ing potential, which for the uniform (staggered) state is  $f_{\mathbf{k}} \Delta \tau_0 i \sigma_y$  ( $f_{\mathbf{k}} \Delta \tau_z i \sigma_y$ ), where  $f_{\mathbf{k}}$  is an even-parity form factor.

In the pseudospin basis, the uniform and staggered pairing potentials are

$$\Delta f_{\mathbf{k}} \tau_0 i \sigma_y \rightarrow \Delta f_{\mathbf{k}} i s_y \quad (4)$$

$$\Delta f_{\mathbf{k}} \tau_z i \sigma_y \rightarrow \pm (\hat{\epsilon}_{zx,\mathbf{k}} s_x + \hat{\epsilon}_{zy,\mathbf{k}} s_y) \Delta f_{\mathbf{k}} i s_y. \quad (5)$$

The odd-parity staggered state is transformed into a helical pseudospin-triplet state, with reduced gap magnitude  $\sqrt{\hat{\epsilon}_{zx,\mathbf{k}}^2 + \hat{\epsilon}_{zy,\mathbf{k}}^2} |\Delta f_{\mathbf{k}}|$  and opposite sign in each band. The reduced gap magnitude of the staggered state is due to interband pairing, implying that this state has a lower transition temperature ( $T_c$ ) than the uniform state. In the weak-coupling limit the  $T_c$  of the staggered state is determined by an effective coupling constant which is smaller than that of the uniform state by  $\langle \hat{\epsilon}_{zx,\mathbf{k}}^2 + \hat{\epsilon}_{zy,\mathbf{k}}^2 \rangle_{\text{FS}} = \langle \tilde{\alpha}_{\mathbf{k}}^2 / (1 + \tilde{\alpha}_{\mathbf{k}}^2) \rangle_{\text{FS}}$  where the average is taken over the Fermi surface [22]. Due to the exponential sensitivity of  $T_c$  on the coupling constant, the ratio  $\tilde{\alpha}_{\mathbf{k}}$  must be larger than unity for  $T_c$  of the staggered and uniform states to be comparable.

The projection onto the pseudospin basis reveals the essential physics of the field-induced transition. Since the same interaction mediates pairing in both channels, the generically smaller gap opened by the staggered state implies that it has the lower  $T_c$  at zero field. However, whereas the uniform state is Pauli limited (albeit with an enhanced upper critical field due to the reduced effective  $g$  factor [15]), the staggered state is not Pauli limited for a  $c$ -axis field, since the effective pseudospin Zeeman field is perpendicular to the  $\vec{d}$ -vector of the pseudospin triplet state. Thus, a field-induced transition occurs when a  $c$ -axis field suppresses the uniform state below the  $T_c$  of the staggered state.

The key parameter that underlies both the  $T_c$  of the staggered state and the response of the uniform state to  $c$ -axis fields is  $\tilde{\alpha}_{\mathbf{k}}$ . Crucially, our  $\mathbf{k} \cdot \mathbf{p}$  analysis shows that  $\tilde{\alpha}_{\mathbf{k}}$  strongly varies across the Brillouin zone in  $\text{CeRh}_2\text{As}_2$

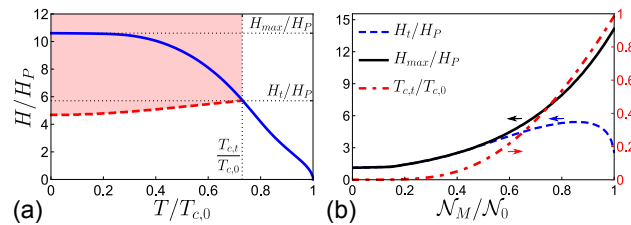


FIG. 1. (a) Phase diagram for  $\mathcal{N}_M = 0.9\mathcal{N}_0$ : the blue line gives the upper critical field of the uniform state, and the red dashed line gives the boundary of the staggered state. The staggered state is realized in the shaded region. (b) The dependence of the upper critical field of the uniform state ( $H_{\max}$ , black solid line) and the critical field ( $H_t$ , blue dashed line) and temperature ( $T_{c,t}$ , red dot-dashed line) at which the field-induced transition occurs as a function of the contribution of the density of states at the M point to the total density of states. The field strengths are expressed in terms of the Pauli limiting field  $H_P \approx 1.25k_B T_{c,0}$ .

due to the NS crystal symmetry. In particular, although it vanishes upon approaching the  $\Gamma$  point,  $\tilde{\alpha}_{\mathbf{k}}$  diverges towards the M-A Dirac line due to the vanishing inter-sublattice terms, as indicated in Table I. More generally, it diverges on the Brillouin zone edges. Thus, large values of  $\tilde{\alpha}_{\mathbf{k}}$  are generically expected for Fermi surfaces sufficiently near the zone edge. In  $\text{CeRh}_2\text{As}_2$ , the field-induced transition occurs at  $T_{c,t} \approx 0.7T_{c,0}$ , where  $T_{c,0}$  is the zero-field transition temperature, implying that  $\tilde{\alpha}_{\mathbf{k}} \approx 3.5$  at the Fermi energy. Our theory shows that such ratios are possible if states near the Brillouin zone edge make a significant contribution to the DOS at the Fermi energy. Previous theoretical studies of  $\text{CeRh}_2\text{As}_2$  have assumed Fermi surfaces near the  $\Gamma$  point, where the enhancement of  $\tilde{\alpha}_{\mathbf{k}}$  due to the NS symmetry is not apparent [4–6]; as in similar treatments of symmorphic lattices [18–21], these theories require an unexpectedly large SOC strength to explain the field-induced transition.

It is instructive to contrast our results with previous results in  $I$ -symmetric 2D Ising superconductors [23–25] and a toy model of a 1D NS zig-zag chain [26]. In the Ising systems, a symmetry-required divergence of the ratio  $\tilde{\alpha}_{\mathbf{k}}$  occurs for band representations with angular momentum  $j_z = \pm 3/2$  at certain points in the 2D Brillouin zone, which strongly enhances the Pauli limit field for in-plane fields. Our result is more general, however, as the divergent  $\tilde{\alpha}_{\mathbf{k}}$  occurs on a 2D manifold of the 3D Brillouin zone, and holds for all band representations. In the zig-zag chain, the stability of an odd-parity state similar to that discussed here is found to be enhanced when the 1D FS is near the zone edge [26]. Although the corresponding ratio  $\tilde{\alpha}_{\mathbf{k}}$  does take a maximum at the zone-edge, it does not diverge as in our model. Consequently, the NS spin texture mechanism we examine is a more general route to enhancing the effect of SOC.

*Two-pocket model*—While Fermi surfaces near the zone edge favor a field-induced transition, it is likely that they will appear together with other Fermi surfaces near the

zone center where the parameter  $\tilde{\alpha}_{\mathbf{k}}$  is small. To examine the sensitivity of our theory to the presence of these additional Fermi surfaces, we consider a model of  $\text{CeRh}_2\text{As}_2$  with two cylindrical Fermi pockets centered on the  $\Gamma$ -Z and M-A Dirac lines, fixing  $|\tilde{\gamma}_{\mathbf{k}}^z| = 0.9$  and  $0.1|\hat{k}_x\hat{k}_y|$  on the two Fermi surfaces, corresponding to small and large values of  $\tilde{\alpha}_{\mathbf{k}}$ , respectively. The momentum-dependence of the effective  $g$ -factor near the M-A Dirac line reflects the NS symmetry-enforced spin texture at the zone boundary. Assuming an intrasublattice pairing interaction, we use standard techniques to construct the field-temperature phase diagram, see the SM for details [17]. For simplicity we assume an  $s$ -wave form factor, i.e.  $f_{\mathbf{k}} = 1$ , but our results are robust to other choices.

In Fig. 1(a), we present a phase diagram which qualitatively agrees with that observed in  $\text{CeRh}_2\text{As}_2$ . Since we only consider the Zeeman effect, the upper critical field of the staggered state is infinite, and so the right-most boundary of the staggered state is vertical; including orbital effects will give a finite upper critical field [2], but does not qualitatively alter our theory. Fig. 1(a) was found by setting the M-A pocket DOS at 90% the total DOS. In Fig. 1(b) we examine the consequences of varying this M-A pocket DOS for the upper critical field of the uniform state, and the field strength and temperature at which the transition into the staggered state occurs. The field-induced transition is strongly enhanced as the contribution of the M-A pocket to the DOS increases, with the even- and odd-parity states near-degenerate when this is the only Fermi surface. Importantly, the field-induced transition occurs at an observable temperature  $T_{c,t} > 0.1T_{c0}$  if the M-A pocket makes up at least half of the DOS.

*DFT results*—DFT calculations and analysis were carried out to explore the possibility that the Fermi surface of  $\text{CeRh}_2\text{As}_2$  contains regions near the zone-edge and to verify that the states at the zone-edge exhibit the spin polarization found above. As shown in the SM [17], the Fermi surface (shown in Fig. S1a) predicted by the DFT bands consists of four pockets about the A point that do not intersect the zone edge, and portions about the  $\Gamma$ -Z line, representing  $\sim 53\%$  of the DOS, in agreement with [6]. This Fermi surface is unlikely to be consistent with the observed odd-parity state.

The experimental heat jump at the superconducting transition temperature suggest fermion masses a factor 100-1000 larger than the bare electron mass, implying that the Ce  $4f$  electrons are itinerant. The standard DFT results are inconsistent with this enhanced effective mass. To address this, we have employed a renormalized band structure approach similar to that pioneered by Zwicky [27, 28]. Fig. 2a shows the resulting band structure; the corresponding Fermi surface, Fig. 2b, has a DOS 10 times larger than standard DFT and agrees with that found in Ref. [29]. Moreover, the pockets at the zone boundary account for 80% of the total DOS, consistent with the observed odd-parity state. In the SM, we show

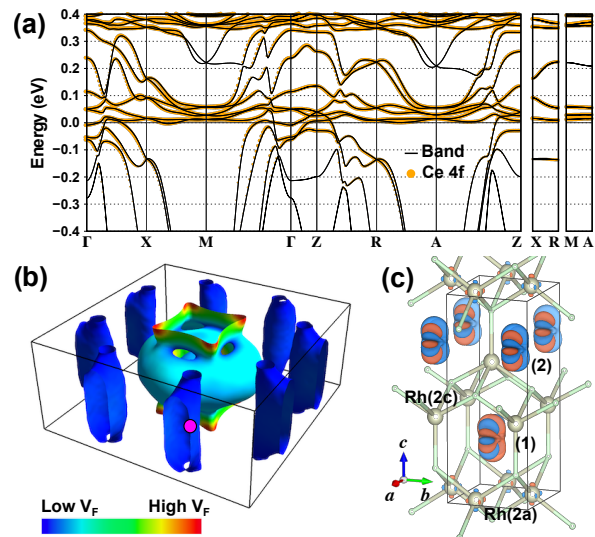


FIG. 2. (a) Bands including  $4f$  electron correlations through a renormalized band structure approach with Ce  $4f$  weight represented by orange dots. (b) Fermi surface for (a). (c)  $x$ -component spin density distribution of the doubly degenerate bands at a point on zone edge marked by the pink circle in (b). Red/blue represents positive/negative spin density.

that with different choices of renormalizations, the DOS can be further increased (with similar Fermi surfaces), and also explore the effects on the band structure from several other scenarios within DFT. Figure 2(c) shows the  $S_x$  spin density arising from a Kramers pair on the zone boundary; the integrated spin density around each atom is non-vanishing only for  $S_x$  and is opposite on the two sublattices, in agreement with the symmetry-based arguments presented above.

*Discussion and conclusions*—Our key result is that the NS  $P4/nmm$  structure of  $\text{CeRh}_2\text{As}_2$  enables the SOC structure required to stabilize an odd-parity superconducting state under field and to enhance the critical field along the  $c$ -axis. It is natural to ask if there exist other materials with the same structure for which this is also the case. Remarkably, there exist experimental results on superconducting FeSe, which also crystallizes in a  $P4/nmm$  structure, that suggest similar considerations apply. In particular, Knight shift measurements indicate that there is no change in the spin susceptibility upon entering the superconducting state for the field applied along the  $c$ -axis [30, 31]. Within the framework we have discussed here, this could be explained by a nearly-vanishing  $g$ -factor for a  $c$ -axis Zeeman field due to strong SOC. This implies that the Zeeman coupling only produces a van-Vleck-like spin susceptibility which is largely unchanged by superconductivity [18]. In addition, there exists evidence for an unexplained  $c$ -axis field-induced superconducting phase transition for fields much larger than the Pauli limiting field [32]. The possibility that this transition corresponds to a transition from an even to odd parity phase is currently under investigation.

*Acknowledgements*– MW and TS were supported by the US Department of Energy, Office of Basic Energy Sciences, Division of Materials Sciences and Engineering under Award DE-SC0017632. DCC and PMRB were supported by the Marsden Fund Council from Government funding, managed by Royal Society Te Apārangi. DFA

was supported by the US Department of Energy, Office of Basic Energy Sciences, Division of Materials Sciences and Engineering under Award DE-SC0021971. We acknowledge useful discussions with Manuel Brando, Mark Fischer, Christoph Geibel, Elena Hassinger, Seunghyun Khim, Andy Mackenzie, Igor Mazin, and Manfred Sigrist.

- 
- [1] S. Khim, J. F. Landaeta, J. Banda, N. Bannor, M. Brando, P. M. R. Brydon, D. Hafner, R. Küchler, R. Cardoso-Gil, U. Stockert, A. P. Mackenzie, D. F. Agterberg, C. Geibel, and E. Hassinger, *Science* **373**, 1012 (2021).
- [2] E. G. Schertenleib, M. H. Fischer, and M. Sigrist, *Phys. Rev. Research* **3**, 023179 (2021).
- [3] A. Ptok, K. J. Kapcia, P. T. Jochym, J. Łażewski, A. M. Oleś, and P. Piekarczyk, *Phys. Rev. B* **104**, L041109 (2021).
- [4] D. Möckli and A. Ramires, *Phys. Rev. Research* **3**, 023204 (2021).
- [5] A. Skurativska, M. Sigrist, and M. H. Fischer, *Phys. Rev. Research* **3**, 033133 (2021).
- [6] K. Nogaki, A. Daido, J. Ishizuka, and Y. Yanase, “Topological crystalline superconductivity in locally non-centrosymmetric CeRh<sub>2</sub>As<sub>2</sub>,” (2021), arXiv:2103.08088 [cond-mat.supr-con].
- [7] M. Sato and Y. Ando, *Reports on Progress in Physics* **80**, 076501 (2017).
- [8] K. Gottlieb, C.-Y. Lin, M. Serbyn, W. Zhang, C. L. Smallwood, C. Jozwiak, H. Eisaki, Z. Hussain, A. Vishwanath, and A. Lanzara, *Science* **362**, 1271 (2018).
- [9] A proof is as follows: The matrix elements of the  $j$  spin operator with respect to the pseudospin partners are  $\langle \nu, m | S_j | \nu, m' \rangle = \langle \nu, m | \tilde{M}_x^{-1} \tilde{M}_x S_j \tilde{M}_x^{-1} \tilde{M}_x | \nu, m' \rangle = e_{\nu, m}^* e_{\nu, m'} (-1)^j \langle \nu, m | S_j | \nu, m' \rangle$ , where  $(-1)^j = -1$  (1) for  $j = z, y$  ( $x$ ), and  $e_{\nu, m}$  is the eigenvalue of  $\tilde{M}_x$ . Since the states at the zone boundary have the same eigenvalues, we conclude that all the matrix elements for the  $z$  and  $y$  spin operators are vanishing.
- [10] S. M. Young, S. Zaheer, J. C. Y. Teo, C. L. Kane, E. J. Mele, and A. M. Rappe, *Phys. Rev. Lett.* **108**, 140405 (2012).
- [11] M. I. Aroyo, J. M. Perez-Mato, C. Capillas, E. Kroumova, S. Ivantchev, G. Madariaga, A. Kirov, and H. Wondratschek, *Zeitschrift für Kristallographie* **221**, 15 (2006); M. I. Aroyo, A. Kirov, C. Capillas, J. M. Perez-Mato, and H. Wondratschek, *Acta Crystallographica Section A* **62**, 115 (2006).
- [12] L. Fu and E. Berg, *Phys. Rev. Lett.* **105**, 097001 (2010).
- [13] S. J. Youn, M. H. Fischer, S. H. Rhim, M. Sigrist, and D. F. Agterberg, *Phys. Rev. B* **85**, 220505 (2012).
- [14] Y. Yanase, *Phys. Rev. B* **94**, 174502 (2016).
- [15] Y.-M. Xie, B. T. Zhou, and K. T. Law, *Phys. Rev. Lett.* **125**, 107001 (2020).
- [16] T. Shishidou, H. G. Suh, P. M. R. Brydon, M. Weinert, and D. F. Agterberg, *Phys. Rev. B* **103**, 104504 (2021).
- [17] See the Supplemental Material at .... for details of the DFT calculations, the pseudospin basis, and the calculation of the phase diagram. This includes Ref.s [33–39].
- [18] M. H. Fischer, F. Loder, and M. Sigrist, *Phys. Rev. B* **84**, 184533 (2011).
- [19] T. Yoshida, M. Sigrist, and Y. Yanase, *Phys. Rev. B* **86**, 134514 (2012).
- [20] T. Yoshida, M. Sigrist, and Y. Yanase, *Journal of the Physical Society of Japan* **83**, 013703 (2014).
- [21] M. Sigrist, D. F. Agterberg, M. H. Fischer, J. Goryo, F. Loder, S.-H. Rhim, D. Maruyama, Y. Yanase, T. Yoshida, and S. J. Youn, *Journal of the Physical Society of Japan* **83**, 061014 (2014).
- [22] A. Ramires, D. F. Agterberg, and M. Sigrist, *Phys. Rev. B* **98**, 024501 (2018).
- [23] Y. Nakamura and Y. Yanase, *Phys. Rev. B* **96**, 054501 (2017).
- [24] C. Wang, B. Lian, X. Guo, J. Mao, Z. Zhang, D. Zhang, B.-L. Gu, Y. Xu, and W. Duan, *Phys. Rev. Lett.* **123**, 126402 (2019).
- [25] J. Falson, Y. Xu, M. Liao, Y. Zang, K. Zhu, C. Wang, Z. Zhang, H. Liu, W. Duan, K. He, H. Liu, J. H. Smet, D. Zhang, and Q.-K. Xue, *Science* **367**, 1454 (2020).
- [26] S. Sumita and Y. Yanase, *Physical Review B* **93** (2016).
- [27] G. Zwirgagl, *Advances in Physics* **41**, 203 (1992).
- [28] G. Zwirgagl, *Reports on Progress in Physics* **79**, 124501 (2016).
- [29] D. Hafner, P. Khanenko, E. O. Eljaouhari, R. Küchler, J. Banda, N. Bannor, T. Luhmann, J. F. Landaeta, S. Mishra, I. Sheikin, E. Hassinger, S. Khim, C. Geibel, G. Zwirgagl, and M. Brando, “Possible quadrupole density wave in the superconducting Kondo lattice CeRh<sub>2</sub>As<sub>2</sub>,” (2021), arXiv:2108.06267 [cond-mat.str-el].
- [30] I. Vinograd, S. P. Edwards, Z. Wang, T. Kissikov, J. K. Byland, J. R. Badger, V. Taufour, and N. J. Curro, *Phys. Rev. B* **104**, 014502 (2021).
- [31] S. Molatta, D. Opherden, J. Wosnitza, L. Opherden, Z. T. Zhang, T. Wolf, H. v. Löhneysen, R. Sarkar, P. K. Biswas, H.-J. Grafe, and H. Kühne, *Phys. Rev. B* **104**, 014504 (2021).
- [32] S. Kasahara, T. Watashige, T. Hanaguri, Y. Kohsaka, T. Yamashita, Y. Shimoyama, Y. Mizukami, R. Endo, H. Ikeda, K. Aoyama, T. Terashima, S. Uji, T. Wolf, H. von Löhneysen, T. Shibauchi, and Y. Matsuda, *PNAS* **111**, 16309 (2014).
- [33] M. Weinert, G. Schneider, R. Podloucky, and J. Redinger, *J. Phys. Condens. Matter* **21**, 084201 (2009).
- [34] J. P. Perdew, K. Burke, and M. Ernzerhof, *Phys. Rev. Lett.* **77**, 3865 (1996).
- [35] M. Kawamura, *Computer Physics Communications* **239**, 197 (2019).
- [36] K. Momma and F. Izumi, *Journal of Applied Crystallography* **44**, 1272 (2011).
- [37] C. M. Varma, *Rev. Mod. Phys.* **48**, 219 (1976).
- [38] G. W. Scheerer, Z. Ren, S. Watanabe, G. Lapertot, D. Aoki, D. Jaccard, and K. Miyake, *npj Quantum Materials* **3**, 41 (2018).
- [39] L. Fu, *Phys. Rev. Lett.* **115**, 026401 (2015).

## Appendix A: DFT calculations and analysis

DFT calculations, including spin-orbit, for  $\text{CeRh}_2\text{As}_2$  are carried out using the Full-Potential Linearized Augmented Plane Wave (FLAPW) method [33] with the structural parameters determined by x-ray diffraction [1]. The Perdew-Burke-Ernzerhof form of the generalized gradient approximation [34] is employed for exchange and correlation. The muffin-tin sphere radii are set to 1.4, 1.2, and 1.1 Å for Ce, Rh, and As atoms, respectively. The wave function and potential cutoffs are 16 and 200 Ry, respectively. The Brillouin zone (BZ) is sampled with a  $20 \times 20 \times 10$   $k$ -point mesh during the self-consistent field cycle. A denser  $50 \times 50 \times 25$  mesh is used to determine the Fermi surface, and are visualized by using **FermiSurfer** [35]. The crystal structure and spin density distribution are visualized by using **VESTA** [36].

The calculated Fermi surface of  $\text{CeRh}_2\text{As}_2$  within standard DFT is shown in Fig. S3a, and is in a fair agreement with previous calculations [6]. As described in the main text, this Fermi surface does not account for the experimental high specific heat jump nor intersects the BZ edge where  $\tilde{\alpha}_{\mathbf{k}}$  diverges. The Fermi surface resulting from a shift of the chemical potential by 0.08 eV, Fig. S1b, has tubes around the M-A line as well as other pieces intersecting the zone edge.

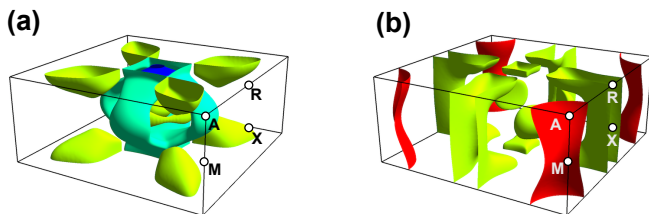


FIG. 3. Fermi surfaces from the standard DFT bands for (a) the calculated Fermi level and (b) for the chemical potential shifted by 0.08 eV.

To partially account for the renormalization/reduction of the bandwidth commonly seen in  $4f$  and heavy fermion materials, we implemented a scheme to manipulate the energy dependence of the logarithmic derivative of the  $4f$  orbitals in the framework of the FLAPW method, an approach closely related to the phase shift technique

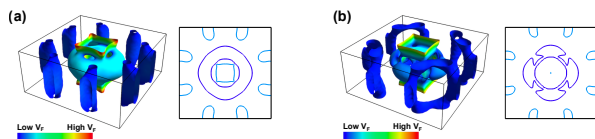


FIG. 4. Fermi surface of  $\text{CeRh}_2\text{As}_2$  with “renormalized”  $\text{Ce } 4f$  bands. (a) and (b) correspond to different choices of renormalization parameters, and provide enhanced DOS at the chemical potential 10 and 20 times larger, respectively, than the bare DFT. For each case, a 3D view (color code shows Fermi velocity) and a  $k_z=0$  section (two colors stand for two different bands) are shown.

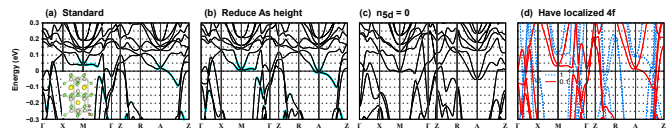


FIG. 5. Electronic band structure of  $\text{CeRh}_2\text{As}_2$ . (a) Standard calculation using the experimental structural parameters. Cyan dots give weight of the  $4d_{xy}$  orbital from the  $2a$ -site Rh (between As atoms). Inset: an illustrative view of crystal structure where Ce, Rh, and As atoms are shown by yellow, gray, and green spheres, respectively. (b) The heights of the As layers sitting above and below the Rh  $2a$  layer are reduced by  $0.05 \text{ \AA}$  from the experimental value  $1.34 \text{ \AA}$ . (c) Positive infinite potential on the Ce  $5d$  orbitals to illustrate  $5d$ - $4f$  valence fluctuation. The  $5d$  electrons (0.70 electrons within a Ce-nucleus centered sphere of radius  $1.4 \text{ \AA}$ ) are eliminated from the occupied levels while the  $4f$  count is increased by 0.54. (d) Localized (core)  $4f$  states for 1 or 0.1  $4f$  electrons to illustrate the effects of localization and  $f^1 \rightarrow f^0$  mixed valence.

used in Ref. [29]. Methodological details will be presented elsewhere. The resulting calculated Fermi surface in Fig. S4(a) [Fig. 2(b) of the main text] closely resembles that in Ref. 29 with six tubes attached to the BZ edge. The total DOS at the Fermi energy is enhanced by a factor of 10 compared to the bare DFT DOS. Fig. S4(b), obtained from another choice of renormalization parameters, shows stronger DOS enhancement, now a factor of 20. The near-edge elements are maintained yet these tubes are now connected at  $k_z = \pm\pi$  plane. In both cases (and with other choices, not shown here), the Fermi surface elements near the BZ edge constitute 80-90% of the total DOS with very low Fermi velocity.

In addition, we examine other possible scenarios, within standard DFT, that alter the relative energies of the bands and provide Fermi surface elements near the BZ edge. The standard DFT calculation shows that the Ce  $4f$  states predominantly hybridize with the conduction Rh  $4d$  bands. In particular, the bottom of the conduction band around the M-A Dirac line of the Brillouin zone is of particular interest since this band, having Ce  $4f$  contributions, shows large Rashba-type band splitting. This state is built up of Rh  $xy$  (and  $z^2$ ) orbitals on the  $2a$  site [the site sandwiched by As atoms; see inset of Fig. S5(a)] antibonded to As  $p$  states. Therefore, the energy position of this band (which at  $M$  point is located about 0.05 eV above the Fermi level) is sensitive to the As-layer height relative to the Rh  $2a$  layer; as demonstrated in Figure S5(b), when the As height is slightly reduced (by  $0.05 \text{ \AA}$ ), this band moves down to the Fermi level. The energy position of this  $4f$ -hybridized band is also sensitive to the mixed valent and localized/delocalized nature of the  $4f$  orbital [37, 38]. Figure S5(c) shows the effect of Ce  $5d$ - $4f$  ( $f^1 \rightarrow f^2$ ) valence fluctuation, which is simulated by adding infinite potential on the  $5d$  state. To mimic localized  $4f$  orbitals and  $f^1 \rightarrow f^0$  fluctuations, the  $4f$  states are treated as core electrons (with the valence states properly orthog-

onalized), and are shown in Fig. S5(d). In all of these cases, the bands around M-A near the chemical potential are common features, although the exact position relative to the chemical potential does vary. Importantly, the robustness of these features implies that the essential physics of the staggered Rashba splitting about the M-A Dirac line near the chemical potential remains unchanged.

### Appendix B: Pseudospin basis

The defining feature of the pseudospin index is that it transforms like a spin under inversion and time-reversal symmetry. That is, letting  $\{|\mathbf{k}, b, \uparrow\rangle, |\mathbf{k}, b, \downarrow\rangle\}$  be the pseudospin basis at momentum  $\mathbf{k}$  in band  $b$ , we have the operation of inversion

$$P|\mathbf{k}, b, \uparrow\rangle = |-\mathbf{k}, b, \uparrow\rangle, \quad P|\mathbf{k}, b, \downarrow\rangle = |-\mathbf{k}, b, \downarrow\rangle, \quad (\text{B1})$$

$$\psi_{\mathbf{k},+, \uparrow} = \begin{pmatrix} -e^{-\frac{i\xi_{\mathbf{k}}}{2}} \cos\left(\frac{\chi_{\mathbf{k}}}{2}\right) \cos\left(\frac{\omega_{\mathbf{k}}}{2}\right) \\ -e^{-\frac{1}{2}i(\xi_{\mathbf{k}}-2\phi_{\mathbf{k}})} \sin\left(\frac{\chi_{\mathbf{k}}}{2}\right) \cos\left(\frac{\omega_{\mathbf{k}}}{2}\right) \\ -e^{\frac{i\xi_{\mathbf{k}}}{2}} \cos\left(\frac{\chi_{\mathbf{k}}}{2}\right) \sin\left(\frac{\omega_{\mathbf{k}}}{2}\right) \\ e^{\frac{1}{2}i(\xi_{\mathbf{k}}+2\phi_{\mathbf{k}})} \sin\left(\frac{\chi_{\mathbf{k}}}{2}\right) \sin\left(\frac{\omega_{\mathbf{k}}}{2}\right) \end{pmatrix}$$

$$\psi_{\mathbf{k},-, \uparrow} = \begin{pmatrix} -ie^{-\frac{i\xi_{\mathbf{k}}}{2}} \text{sgn}(\xi_{\mathbf{k}}) \cos\left(\frac{\chi_{\mathbf{k}}}{2}\right) \sin\left(\frac{\omega_{\mathbf{k}}}{2}\right) \\ ie^{-\frac{1}{2}i(\xi_{\mathbf{k}}-2\phi_{\mathbf{k}})} \text{sgn}(\xi_{\mathbf{k}}) \sin\left(\frac{\chi_{\mathbf{k}}}{2}\right) \sin\left(\frac{\omega_{\mathbf{k}}}{2}\right) \\ ie^{\frac{i\xi_{\mathbf{k}}}{2}} \text{sgn}(\xi_{\mathbf{k}}) \cos\left(\frac{\chi_{\mathbf{k}}}{2}\right) \cos\left(\frac{\omega_{\mathbf{k}}}{2}\right) \\ ie^{\frac{1}{2}i(\xi_{\mathbf{k}}+2\phi_{\mathbf{k}})} \text{sgn}(\xi_{\mathbf{k}}) \sin\left(\frac{\chi_{\mathbf{k}}}{2}\right) \cos\left(\frac{\omega_{\mathbf{k}}}{2}\right) \end{pmatrix}$$

where the angles are defined in terms of the coefficients of the general Hamiltonian as

$$\xi_{\mathbf{k}} = \arctan\left(\frac{\epsilon_{y0,\mathbf{k}}}{\epsilon_{x0,\mathbf{k}}}\right) \quad (\text{B8})$$

$$\omega_{\mathbf{k}} = \arctan\left(\frac{\sqrt{\epsilon_{x0,\mathbf{k}}^2 + \epsilon_{y0,\mathbf{k}}^2}}{\epsilon_{zz,\mathbf{k}}}\right) \quad (\text{B9})$$

$$\chi_{\mathbf{k}} = \arctan\left(\frac{\sqrt{\epsilon_{zx,\mathbf{k}}^2 + \epsilon_{zy,\mathbf{k}}^2}}{\sqrt{\epsilon_{x0,\mathbf{k}}^2 + \epsilon_{y0,\mathbf{k}}^2 + \epsilon_{zz,\mathbf{k}}^2}}\right) \quad (\text{B10})$$

$$\phi_{\mathbf{k}} = \arctan\left(\frac{\epsilon_{zy,\mathbf{k}}}{\epsilon_{zx,\mathbf{k}}}\right) \quad (\text{B11})$$

Note that the appearance of  $\text{sgn}(\xi_{\mathbf{k}})$  in the definition of

and time-reversal

$$T|\mathbf{k}, b, \uparrow\rangle = -|-\mathbf{k}, b, \downarrow\rangle, \quad T|\mathbf{k}, b, \downarrow\rangle = |-\mathbf{k}, b, \uparrow\rangle. \quad (\text{B2})$$

It is furthermore often convenient to adopt a pseudospin basis where the pseudospin has the same transformation properties as the electronic spin under the point group operations, a so-called manifestly covariant Bloch basis (MCBB) [39]. Consider a symmetry operation  $g$  of the point group such that

$$U_g H_0(\mathbf{k}) U_g^\dagger = H_0(g\mathbf{k}), \quad (\text{B3})$$

where  $U_g$  is the unitary matrix for the symmetry operation in the four-component basis. The eigenvectors  $\phi_{\mathbf{k},\pm,s}$  define an MCBB if the matrix with columns composed of these vectors,

$$\Psi_{\mathbf{k}} = (\psi_{\mathbf{k},+, \uparrow}, \psi_{\mathbf{k},+, \downarrow}, \psi_{\mathbf{k},-, \uparrow}, \psi_{\mathbf{k},-, \downarrow}), \quad (\text{B4})$$

satisfies

$$\Psi_{g\mathbf{k}}^\dagger U_g \Psi_{\mathbf{k}} = s_0 \otimes u_g, \quad (\text{B5})$$

where  $u_g$  is the equivalent symmetry operation for a spin-1/2 system.

We adopt the following pseudospin basis for our model

$$\psi_{\mathbf{k},+, \downarrow} = \begin{pmatrix} -e^{-\frac{1}{2}i(\xi_{\mathbf{k}}+2\phi_{\mathbf{k}})} \sin\left(\frac{\chi_{\mathbf{k}}}{2}\right) \sin\left(\frac{\omega_{\mathbf{k}}}{2}\right) \\ -e^{-\frac{i\xi_{\mathbf{k}}}{2}} \cos\left(\frac{\chi_{\mathbf{k}}}{2}\right) \sin\left(\frac{\omega_{\mathbf{k}}}{2}\right) \\ e^{\frac{1}{2}i(\xi_{\mathbf{k}}-2\phi_{\mathbf{k}})} \sin\left(\frac{\chi_{\mathbf{k}}}{2}\right) \cos\left(\frac{\omega_{\mathbf{k}}}{2}\right) \\ -e^{\frac{i\xi_{\mathbf{k}}}{2}} \cos\left(\frac{\chi_{\mathbf{k}}}{2}\right) \cos\left(\frac{\omega_{\mathbf{k}}}{2}\right) \end{pmatrix} \quad (\text{B6})$$

$$\psi_{\mathbf{k},-, \downarrow} = \begin{pmatrix} ie^{-\frac{1}{2}i(\xi_{\mathbf{k}}+2\phi_{\mathbf{k}})} \text{sgn}(\xi_{\mathbf{k}}) \sin\left(\frac{\chi_{\mathbf{k}}}{2}\right) \cos\left(\frac{\omega_{\mathbf{k}}}{2}\right) \\ -ie^{-\frac{i\xi_{\mathbf{k}}}{2}} \text{sgn}(\xi_{\mathbf{k}}) \cos\left(\frac{\chi_{\mathbf{k}}}{2}\right) \cos\left(\frac{\omega_{\mathbf{k}}}{2}\right) \\ ie^{\frac{1}{2}i(\xi_{\mathbf{k}}-2\phi_{\mathbf{k}})} \text{sgn}(\xi_{\mathbf{k}}) \sin\left(\frac{\chi_{\mathbf{k}}}{2}\right) \sin\left(\frac{\omega_{\mathbf{k}}}{2}\right) \\ ie^{\frac{i\xi_{\mathbf{k}}}{2}} \text{sgn}(\xi_{\mathbf{k}}) \cos\left(\frac{\chi_{\mathbf{k}}}{2}\right) \sin\left(\frac{\omega_{\mathbf{k}}}{2}\right) \end{pmatrix} \quad (\text{B7})$$

the  $-$  band states is ill-defined if  $\xi_{\mathbf{k}} = 0$ ; since  $\xi_{\mathbf{k}} = -\xi_{-\mathbf{k}}$ , however, on this set of measure zero we can define  $\text{sgn}(\xi_{\mathbf{k}}) = 1$  and  $\text{sgn}(\xi_{-\mathbf{k}}) = -1$ .

A key feature of this pseudospin basis is that it converges smoothly to the electronic spin in the limit of vanishing SOC, which is reached when  $\omega_{\mathbf{k}} \rightarrow \frac{\pi}{2}$  and  $\chi_{\mathbf{k}} \rightarrow 0$ . Other important cases are a purely Rashba SOC ( $\epsilon_{zz,\mathbf{k}} = 0$ ), where we have  $\omega_{\mathbf{k}} = \frac{\pi}{2}$ , and a purely Ising SOC ( $\epsilon_{zx,\mathbf{k}} = \epsilon_{zy,\mathbf{k}} = 0$ ) which is characterized by  $\chi_{\mathbf{k}} = 0$ . In the latter case the pseudospin is again equivalent to the electronic spin.

We now consider the projection of the spin operators onto the pseudospin basis of each band:

$$\tau_0 \sigma_x \rightarrow \sin(\omega_{\mathbf{k}}) (\cos(\chi_{\mathbf{k}}) \sin^2(\phi_{\mathbf{k}}) + \cos^2(\phi_{\mathbf{k}})) s_x \quad (\text{B12})$$

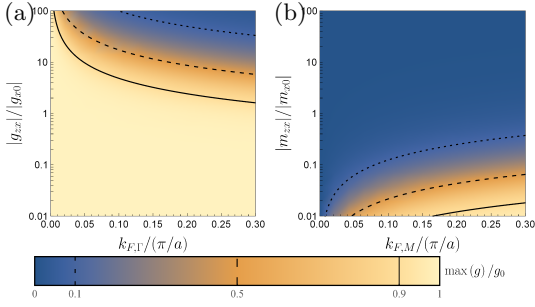


FIG. 6. The dependence of the effective  $g$ -factor magnitude on the  $\Gamma$  point Fermi surface pocket (a) and maximum magnitude on the  $M$  point Fermi surface pocket (b) on the ratio of SOC to interlayer hopping and relevant Fermi wavevector  $k_F$ .

$$+ \sin^2 \left( \frac{\chi \mathbf{k}}{2} \right) \sin(\omega_{\mathbf{k}}) \sin(2\phi_{\mathbf{k}}) s_y \quad (\text{B13})$$

$$+ \sin(\chi_{\mathbf{k}}) \cos(\omega_{\mathbf{k}}) \cos(\phi_{\mathbf{k}}) s_z \quad (\text{B14})$$

$$\tau_0 \sigma_y \rightarrow \sin^2 \left( \frac{\chi \mathbf{k}}{2} \right) \sin(\omega_{\mathbf{k}}) \sin(2\phi_{\mathbf{k}}) s_x \quad (\text{B15})$$

$$+ \sin(\omega_{\mathbf{k}}) (\sin^2(\phi_{\mathbf{k}}) + \cos(\chi_{\mathbf{k}}) \cos^2(\phi_{\mathbf{k}})) s_y \quad (\text{B16})$$

$$+ \sin(\chi_{\mathbf{k}}) \cos(\omega_{\mathbf{k}}) \sin(\phi_{\mathbf{k}}) s_z \quad (\text{B17})$$

$$\tau_0 \sigma_z \rightarrow \cos(\chi_{\mathbf{k}}) s_z \quad (\text{B18})$$

The pseudospin and Zeeman fields are not generally colinear, with the notable exception of a  $c$ -axis Zeeman field. In both the Rashba and Ising limits in-plane and out-of-plane Zeeman fields produce pseudospin fields which are also strictly in-plane and out-of-plane, respectively.

We now turn to the staggered singlet pairing state.

Expressed in the pseudospin basis we have

$$\tau_z i \sigma_y \rightarrow \pm [\sin \chi_{\mathbf{k}} \sin \omega_{\mathbf{k}} (\cos \phi_{\mathbf{k}} \hat{s}_x + \sin \phi_{\mathbf{k}} \hat{s}_y) + \cos \omega_{\mathbf{k}} \hat{s}_z] i \hat{s}_y \quad (\text{B19})$$

Since we have a MCBB, the effective  $\mathbf{d}$ -vector indeed transforms as a state in the  $A_{2u}$  irrep, with  $\mathbf{d}_{\mathbf{k}} \sim a_1(f_y \hat{\mathbf{x}} - f_x \hat{\mathbf{y}}) + a_2 f_{A_{1u}} \mathbf{z}$ , where  $f_{\nu}$  has the transformation properties of a  $p_{\nu}$ -harmonic, whereas  $f_{A_{1u}}$  transforms as  $A_{1u}$ . We note that in the Ising limit the effective  $\mathbf{d}$ -vector is oriented along the  $c$ -axis, whereas in the Rashba limit the  $\mathbf{d}$ -vector is purely in-plane. Comparing this to the projected spin operators, we note the remarkable result that the staggered singlet state is immune to in-plane and out-of-plane fields in the Ising and Rashba limits, respectively. This is a particular feature of the staggered singlet state which makes it generically robust against applied fields.

### Appendix C: Model calculation

In a  $c$ -axis field  $H$ , the free energy of the uniform singlet superconductor relative to the normal state is given by

$$F_S = \mathcal{N}_0 |\Delta_0|^2 \Phi \left( \frac{\Delta}{\Delta_0}, \frac{k_B T}{\Delta_0}, \frac{g \mu_B H}{\Delta_0} \right), \quad (\text{C1})$$

where  $\mathcal{N}_0$  is the total density of state at the Fermi energy,  $\Delta_0$  is the zero temperature and zero field superconducting gap. The latter is explicitly given by

$$\Delta_0 = 2\Lambda \exp \left( - \frac{1}{V_0 \sum_{\nu} \mathcal{N}_{\nu} \langle |f_{\nu, \mathbf{k}}|^2 \rangle_{\nu}} \right) \exp \left( - \frac{\sum_{\nu} \mathcal{N}_{\nu} \langle |f_{\nu, \mathbf{k}}|^2 \log(|f_{\nu, \mathbf{k}}|) \rangle_{\nu}}{\sum_{\nu} \mathcal{N}_{\nu} \langle |f_{\nu, \mathbf{k}}|^2 \rangle_{\nu}} \right), \quad (\text{C2})$$

where  $\Lambda$  is the energy scale for the pairing interaction (the exact magnitude of which does not enter into our calculations),  $V_0$  is the pairing interaction. The  $\nu$  index in Eqn. C2 runs over the Fermi surfaces, and  $\langle \dots \rangle_{\nu}$  denotes the average over the  $\nu$  Fermi surface, with  $\mathcal{N}_{\nu}$  the density of states and  $f_{\nu, \mathbf{k}}$  the form factor of the superconducting gap in Fermi surface  $\nu$ . In Eqn. C1, we have also defined the dimensionless function

$$\Phi(\delta, t, h) = \sum_{\nu} \frac{\mathcal{N}_{\nu}}{\mathcal{N}_0} \int_0^{\infty} dx \left\langle \frac{|f_{\nu, \mathbf{k}}|^2 \delta^2}{\sqrt{x^2 + |f_{\nu, \mathbf{k}}|^2}} - 2t \sum_{\sigma=\pm} \log \left[ \frac{\cosh \left( \frac{\sigma |\tilde{\gamma}_{\nu, \mathbf{k}}^z| h + \sqrt{x^2 + |f_{\nu, \mathbf{k}}|^2} \delta^2}{2t} \right)}{\cosh \left( \frac{\sigma |\tilde{\gamma}_{\nu, \mathbf{k}}^z| h + x}{2t} \right)} \right] \right\rangle_{\nu} \quad (\text{C3})$$

with  $|\tilde{\gamma}_{\nu, \mathbf{k}}^z|$  the (momentum-dependent) effective  $g$ -factor on the  $\nu$  Fermi surface pocket. For the pocket centered about the M-A Dirac line, the effective  $g$ -factor vanishes with the radius of the pocket  $k_{F, MA} \rightarrow 0$ , while for the pocket at the  $\Gamma$ -Z line the effective  $g$ -factor converges to the free electron value as  $k_{F, \Gamma Z} \rightarrow 0$  due to the vanishing of the ratio  $\tilde{\alpha}_{\mathbf{k}}$ . Additionally, the effective  $g$ -factor of the  $M$  point Fermi surface pocket is strongly anisotropic. From our  $\mathbf{k} \cdot \mathbf{p}$  theory at  $k_z = 0$ , the dependence of the effective  $g$ -factors on the model parameters and Fermi pocket size are presented in Fig. S6. Clearly, for a wide parameter range the maximum of the  $g$ -factor for the M-A pocket is typically close to zero, while for the  $\Gamma$ -Z pocket the  $g$ -factor is generally only slightly smaller than  $g_0$ .



The free energy of the staggered singlet (relative to the normal state) is similarly given by

$$F_{S,s} = \mathcal{N}_0 |\Delta_{0,s}|^2 \Phi_s \left( \frac{\Delta}{\Delta_{0,s}}, \frac{k_B T}{\Delta_{0,s}} \right), \quad (\text{C4})$$

where  $\Phi_s$  is related to Eq. C3 by  $\Phi_s(\delta, t) = \Phi(\delta, t, h = 0)$  with the substitution  $|f_{\nu, \mathbf{k}}| \rightarrow \sqrt{r_{\nu, \mathbf{k}}} |f_{\nu, \mathbf{k}}|$  which accounts for the reduced magnitude of the gap on the Fermi surface, with  $r_{\nu, \mathbf{k}}$  the superconducting fitness on band  $\nu$  [22]. The  $c$ -axis magnetic field does not enter this expression since it is not pair breaking for the staggered singlet state, Assuming the pairing interaction  $V_0$  is of equal strength in both the uniform and staggered singlet channels, the pairing potential at zero temperature is

$$\Delta_{0,s} = 2\Lambda \exp \left( - \frac{1}{V_0 \sum_{\nu} \mathcal{N}_{\nu} \langle r_{\nu, \mathbf{k}} |f_{\nu, \mathbf{k}}|^2 \rangle_{\nu}} \right) \exp \left( - \frac{\sum_{\nu} \mathcal{N}_{\nu} \langle r_{\nu, \mathbf{k}} |f_{\nu, \mathbf{k}}|^2 \log(\sqrt{r_{\nu, \mathbf{k}}} |f_{\nu, \mathbf{k}}|) \rangle_{\nu}}{\sum_{\nu} \mathcal{N}_{\nu} \langle r_{\nu, \mathbf{k}} |f_{\nu, \mathbf{k}}|^2 \rangle_{\nu}} \right). \quad (\text{C5})$$

The necessary choice of a specific value for the pairing interaction is the only non-universal aspect of our calculation, as the energy scale  $\Lambda$  is irrelevant since the staggered singlet free energy can be expressed in terms of the ratio between the two gap magnitudes, and we assume an intermediate pairing interaction strength of  $V_0 \mathcal{N}_0 = 0.3$ .

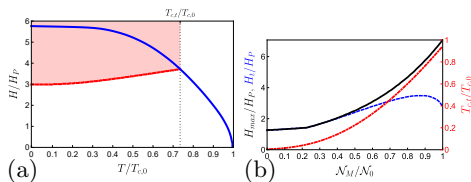


FIG. 7. Variation of the effective  $g$ -factor magnitudes: (a) The phase diagram for  $\mathcal{N}_M = 0.9\mathcal{N}_0$ , the blue line gives the upper critical field of the uniform state, and the red dashed line gives the boundary of the staggered state (shaded). (b) Plot showing the dependence of the upper critical field of the uniform state ( $H_{\max}$ ) and the critical field ( $H_t$ ) and temperature ( $T_{c,t}$ ) at which the field-induced transition occurs as a function of the contribution of the density of states at the  $M$  point to the total density of states, assuming an equal pairing interaction strength in both channels, and  $g_{\Gamma} = 0.8g_0$  and  $\max(g_M) = 0.2g_0$ .

We minimize the free energy of the uniform and staggered singlet states, Eqs. C1 and C4, and compare the two over the range of temperature and field to obtain the phase diagram. Reasonable variation of the effective  $g$ -factor magnitudes or interaction strength does not qualitatively alter the phase diagram. However, the reduction of the effective  $g$ -factor at the  $\Gamma$  point and enhancement at the  $M$  point in Fig. S 7 reduces the critical field magnitudes, but does not qualitatively alter the phase diagram otherwise.

We can additionally consider a model with Fermi surface pockets around the M-A and X-R Dirac lines, where the latter pocket has a strongly anisotropic effective  $g$ -factor which is independent of  $k_{F, \text{XR}}$ . For reasonable ratios of the SOC strength and interorbital hopping in

tegral it has a maximum value close to the bare  $g_0$ , although the anisotropy significantly reduces the average value of the effective  $g$ -factor. In this model, we find that the M-A pocket is still the most significant contributor to the stability of the staggered singlet state, but that

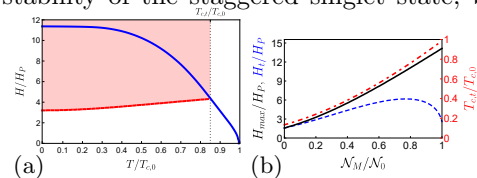


FIG. 8. Two pocket model with pockets at M-A and X-R: (a) The phase diagram for  $\mathcal{N}_M = 0.9\mathcal{N}_0$ , the blue line gives the upper critical field of the uniform state, and the red dashed line gives the boundary of the staggered state (shaded). (b) Plot showing the dependence of the upper critical field of the uniform state ( $H_{\max}$ ) and the critical field ( $H_t$ ) and temperature ( $T_{c,t}$ ) at which the field-induced transition occurs as a function of the contribution of the density of states at the  $M$  point to the total density of states, assuming an equal pairing interaction strength in both channels, and  $g_X = 0.9g_0$  and  $\max(g_M) = 0.1g_0$ .

the pocket about X-R is considerably less detrimental to the staggered singlet state than the  $\Gamma$ -Z pocket, due to the smaller average  $g$ -factor in the former. In Fig. S8 we highlight the effect of including an X-R pocket instead of the  $\Gamma$ -Z pocket, and see that the transition to the staggered singlet state generically occurs at a higher value of  $T_{c,t}$ .

As a final demonstration of the generality of the phase diagram of the two pocket model, in Fig. S9 we provide results for an M-A and  $\Gamma$ -Z model but with  $d$ -wave form factors  $f_{\mathbf{k}}$ .

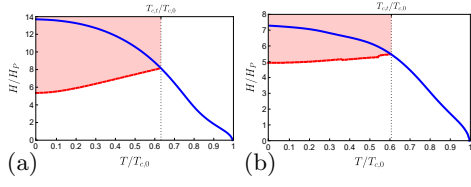


FIG. 9. The phase diagram for  $\mathcal{N}_M = 0.9\mathcal{N}_0$ ,  $g_\Gamma = 0.9g_0$  and  $\max(g_M) = 0.1g_0$  with (a)  $d_{x^2-y^2}$ -wave and (b)  $d_{xy}$ -wave form factors. The blue line gives the upper critical field of the uniform state, and the red dashed line gives the boundary of the staggered state (shaded). Here,  $T_{c,0}$  is the critical temperature for the  $d$ -wave state.